PAPER

Check for updates

Injectable colloidal hydrogel with mesoporous silica nanoparticles for sustained co-release of microRNA-222 and aspirin to achieve innervated bone regeneration in rat mandibular defects†

Lei Lei, [ID][a] Zhongning Liu,[a] Pingyun Yuan,[b] Ronghua Jin,[b] Xiangdong Wang,[b] Ting Jiang [ID] *[a] and Xin Chen [ID] *[b]

Nerve fibers and vessels play important roles in bone formation, and inadequate innervation in the bone defect area can delay the regeneration process. However, there are few studies aiming to promote innervation to engineer bone formation. Here, we report the development of an injectable thermoresponsive mesoporous silica nanoparticle (MSN)-embedded core–shell structured poly(ethylene glycol)-*b*-poly(lactic-*co*-glycolic acid)-*b*-poly(*N*-isopropylacrylamide) (PEG–PLGA–PNIPAM) hydrogel for localized and long-term co-delivery of microRNA-222 and aspirin (ASP) (miR222/MSN/ASP hydrogel). ASP was found to stimulate bone formation as previously reported, and miR222 induced human bone mesenchymal stem cell differentiation into neural-like cells through Wnt/β-catenin/Nemo-like kinase signaling. In a rat mandibular bone defect, injection of the co-delivered MSN hydrogel resulted in neurogenesis and enhanced bone formation, indicating that the present injectable miR222- and ASP-*co*-delivering colloidal hydrogel is a promising material for innervated bone tissue engineering.

1. Introduction

Nerve fibers play a critical role in bone metabolism and bone cell functions as they are widely distributed at a high density in bone tissues.[1,2] Neuromediators have been shown to act on osteoblasts and osteoclasts to modulate bone resorption and formation; it follows that inadequate nerve fibers in the bone defect area can hinder nutrient metabolism, resulting in reduced bone regeneration and poor bone quality.[3,4]

Although innervation is important for regulating bone formation, only a few studies have investigated the potential of enhancing neurogenesis in engineered bone.[5] Studies have mostly focused on utilizing nerve tracts or bone implant materials for bone engineering application by neurotization.[6–8]

[a] *Department of Prosthodontics, Peking University School and Hospital of Stomatology, National Clinical Research Center for Oral Diseases, National Engineering Laboratory for Digital and Material Technology of Stomatology, Beijing Key Laboratory of Digital Stomatology, 22, Zhongguancun South Avenue, Haidian District, Beijing 100081, China. E-mail: jt_ketizu@163.com*

[b] *School of Chemical Engineering and Technology, Shaanxi Key Laboratory of Energy Chemical Process Intensification, Institute of Polymer Science in Chemical Engineering, Xi'an Jiao Tong University, Xi'an 710049, China. E-mail: chenx2015@xjtu.edu.cn*

† Electronic supplementary information (ESI) available: Additional δ potential measurements, surface charge, scanning electron micrographs and immunohistochemical staining of CGRP are supplied. See DOI: 10.1039/c9tb00025a

These approaches for achieving innervated bone regeneration have their drawbacks: implantation surgery and nerve fiber dissociation may exacerbate the original injury. We previously utilized brain-derived neurotrophic factor combined with β-tricalcium phosphate (TCP) and human bone mesenchymal stem cells to achieve neurogenesis-associated ectopic bone formation in nude mice using human bone marrow-derived mesenchymal stem cells (hBMSCs).[9] However, the use of recombinant growth factors is expensive and may be associated with safety issues as a result of non-specific effects.[10,11] Therefore, there is an urgent need for engineering innervated bone with less trauma using biological safe approaches.

Micro-RNAs (miRNAs) are endogenous small noncoding RNAs (∼22 nucleotides long) that modulate gene expression *via* post-transcriptional processing. Various miRNAs have been shown to modulate neurobiological processes including neurite outgrowth, synaptogenesis, and neural plasticity.[12] Although they have been applied in tissue engineering and the treatment of various diseases, miRNA-based approaches for inducing neuralization in regenerated bone have not been reported. Studies have shown that miR222 is capable of promoting nerve outgrowth from neurons,[13] and improving nerve regeneration following nerve injury.[14] The findings demonstrated that miR222 is highly associated with neural differentiation, with potential applications in improving innervation in engineered bone tissue.

Aspirin (ASP) has long been used as a non-steroidal anti-inflammatory drug for the treatment of moderate pain, inflammation, cardiovascular diseases, and even cancer.[15–17] In recent years, ASP has been shown to enhance the osteogenic potential and promote the proliferation of stem cells.[18–21] A previous study has also demonstrated that ASP improves bone regeneration via the inhibition of immune cells under inflammatory conditions.[22] In the present study, ASP is used for reducing inflammation in the bone defect area and enhancing bone formation.
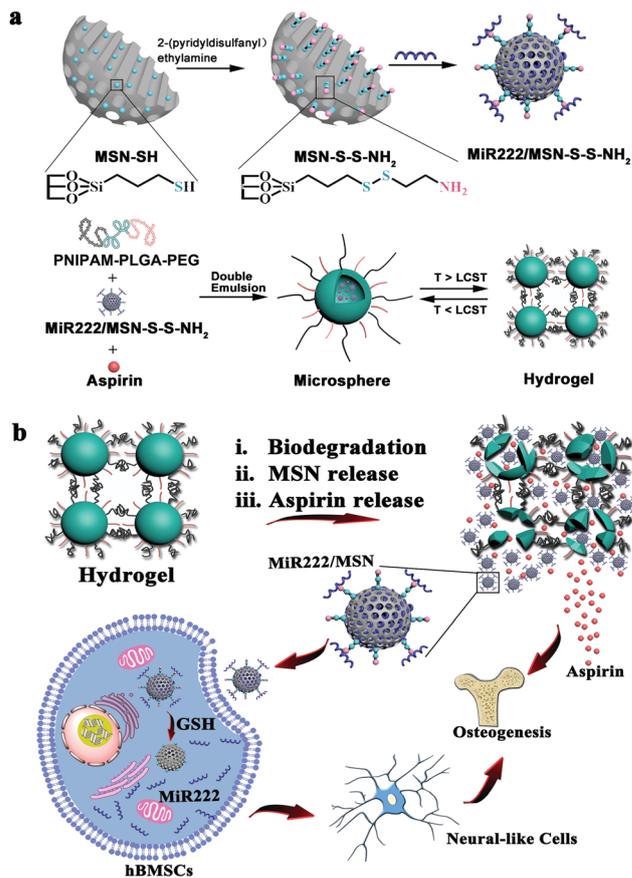
We hypothesize that co-delivery of miR222 and ASP to the rat mandibular defect area, results in the induction of neural differentiation of stem cells by miR222 and the generation of a pro-osteogenic microenvironment by ASP, leading to innervated bone formation. Therefore, a delivery system is required for simultaneously long-term and effective co-release of miR222 and ASP at the bone defect site.

In the present study, we fabricated an injectable thermo-responsive mesoporous silica nanoparticle (MSN)-embedded core–shell structured poly(ethylene glycol)-b-poly(lactic-co-glycolic acid)-b-poly(N-isopropylacrylamide) (PEG–PLGA–PNIPAM) hydrogel for localized and long-term co-delivery of miR222 and ASP in the form of a miR222/MSN/ASP hydrogel, with PLGA serving as the core and PEG/PNIPAM as the shell (Scheme 1). A two-stage reaction was responsible for sustainability and effective transfection of miR222 and ASP into cells (Scheme 1b, in the first stage, miR222/MSN complexes and ASP escape from the microsphere-based hydrogel and are endocytosed by cells; in the second stage, miR222s are released from MSNs). Using a rat mandibular defect model, the miR222/ASP MSNs hydrogel was injected and the hypothesized synergistic function of miR222 and ASP was confirmed by the formation of new bone tissue with neural-like structures in the bone defect area, demonstrating that this strategy is effective for engineering innervated bone tissue.

2. Results and discussion

2.1 miR222 promotes neural differentiation of hBMSCs in vitro by targeting Nemo-like kinase (NLK)

The hBMSCs were collected from excised mandibular cancellous bone during orthognathic surgery and cultured. The multipotency of these cells was demonstrated in our previous study.[23] Following transfection with miR222 mimic and neural induction, hBMSCs developed a branched morphology similar to that of neurons, indicating that miR222 can induce the differentiation of hBMSCs into neural-like cells (Fig. 1a). To confirm this result, we analyzed the cells for expression of neuronal markers including microtubule-associated protein (MAP)2, nerve growth factor (NGF), and neural/glial antigen (NG)2 by quantitative real-time polymerase chain reaction (qRT-PCR), and found that three genes were more highly expressed in cells transfected with miR222 mimic than in the negative control (NC) or inhibitor-treated group. Additionally, the protein levels of neural proteins, including β-tubulin III (Tuj1), neural/glial antigen (NG)2, and glial fibrillary acidic protein (GFAP), were markedly increased in the mimic-transfected group as detected by western
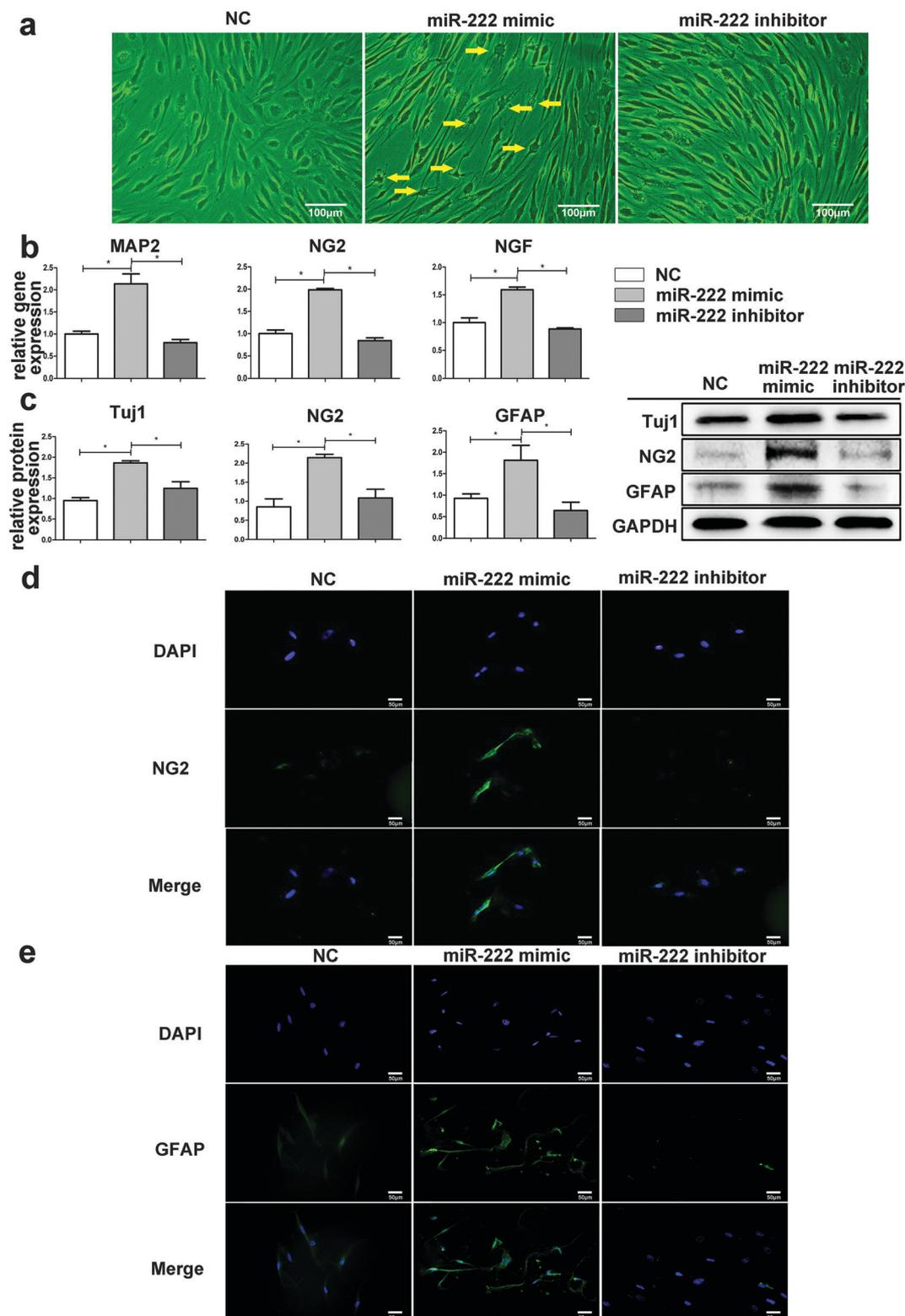

Scheme 1 (a) Fabrication process of thermo-responsive miR222/MSN/ASP-embedded core−shell microspheres. (b) Illustration of miR222 and ASP released from miR222/MSN/ASP-embedded core−shell microspheres, their cellular uptake and biological function.
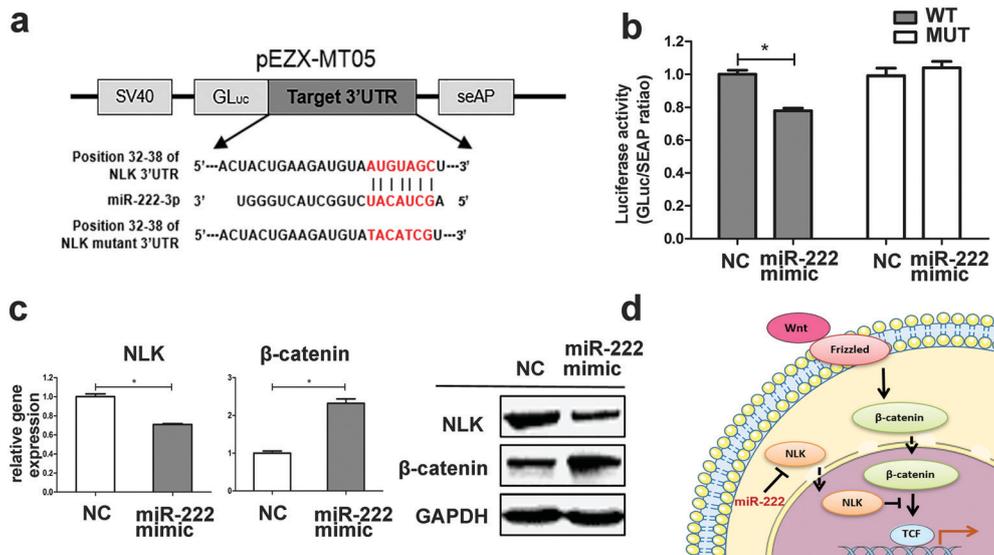
blotting, which is in agreement with the qRT-PCR results (Fig. 1c). Immunofluorescence analysis confirmed the overexpression of NG2 and GFAP in miR222-overexpressing cells (Fig. 1d and e). These results demonstrate that miR222 positively regulates neural differentiation of hBMSCs.

To investigate the target gene of miR222, we carried out a luciferase reporter assay using pEZX-MT05 plasmid containing putative binding sites for NLK, which were predicted using the TargetScan database (http://www.targetscan.org/vert_70/). NLK is a potential target of miR222 and an inhibitor of Wnt/β-catenin signaling, which plays as a vital role in neuronal differentiation.[24–27] Compared with that in the NC group, luciferase activity was decreased in miR222 mimic transfected cells, whereas no effect was observed upon transfection of a mutant plasmid (Fig. 2a and b). The downregulation of the NLK transcript and upregulation of β-catenin in the miR222 mimic group was confirmed by qRT-PCR assay. NLK protein level was decreased by overexpression of miR222 with a corresponding increase in the upstream factor β-catenin, as determined by western blotting. The mechanism underlying the induction of neural differentiation induction by miR222 is schematically illustrated in Fig. 2d.

miR222 has been reported to promote nerve outgrowth from neurons,[13] and improve nerve regeneration after nerve injury,[14] in

This journal is © The Royal Society of Chemistry 2019

J. Mater. Chem. B, 2019, 7, 2722–2735 | 2723

Fig. 1 (a) Branched and neural-like morphology of hBMSCs in the miR222 mimic group (yellow arrow). (b) Expression of neuronal markers MAP2 and NG2 and NGF in hBMSCs of the miR222 mimic were elevated, comparing with NC, and inhibitor group as determined by qRT-PCR. (c) Western blot analysis of the neuronal proteins Tuj1, NG2, and GFAP were increased in the miR222 mimic group, comparing with NC, and inhibitor group, and fold change of each protein relative to that in the NC group was quantified. (d and e) Immunofluorescence detection of NG2 (d) and GFAP (e) proteins in hBMSCs were the strongest in miR222 mimic group; *$P < 0.05$ ($n = 3$).

2724 | J. Mater. Chem. B, 2019, 7, 2722–2735

This journal is © The Royal Society of Chemistry 2019

Fig. 2 (a) Construction of pEZX-NLK WT and MUT luciferase reporter plasmids. (b) Luciferase activity was reduced in 293T cells transfected with NLK-WT plasmid and miR222 mimic compared with that in the cells transfected with miR-NC. (c) NLK and β-catenin expression after transfection of miR222 mimic and NC as determined by qRT-PCR and western blotting. (d) Schematic illustration of miR222 targeting the NLK gene and positively regulating canonical WNT signaling; *$P < 0.05$ ($n = 3$).

addition, it is over-expressed in fully differentiated PC12 neuro-blastic cells and down-regulated in neurodegenerative diseases.[28–30] More importantly, a recent study using biocompatible cationic polymer delivering microRNA-222 promoted nerve regeneration after sciatic nerve crush.[31] Based on these findings, we further explored the role of miR222 in stem cell neural differentiation and aimed to identify the pathway involved in order to utilize miR222 in bone engineering. The results in Fig. 1c suggested that the untransfected cells expressed Tuj1 protein, this unexpected finding may attribute to the fact that all three groups of cells underwent neural introduction, Tuj1 is among one of the earliest markers in neural development,[32] therefore, Tuj1 expression may be induced during 12 days of neural induction *in vitro*. In general, the expression level of neural markers in the NC, miR222 mimic and inhibitor groups was in consistent with our expected results.

In Fig. 2b, luciferase activity was assayed using 293T cells derived from the HEK 293 cell line, which has been commonly used for transfection as it is efficiently transfectable with DNA and enables high levels of protein production (ATCC, www.atcc.org/products/all/CRL-11268). The WNT/β-catenin pathway was reported to play a positive role in neuronal differentiation and nerve development,[33–35] and NLK is commonly known as a negative regulator in the canonical WNT signaling pathway through phosphorylation of TCF/LEF family transcription factors.[36] As suggested by our results, through binding with the inhibitive factor NLK, miR222 promoted the neural differentiation of hBMSCs *via* positive regulation of WNT/β-catenin pathway.

2.2 Fabrication of MSNs for microRNA delivery and evaluation of miR222 loading capacity
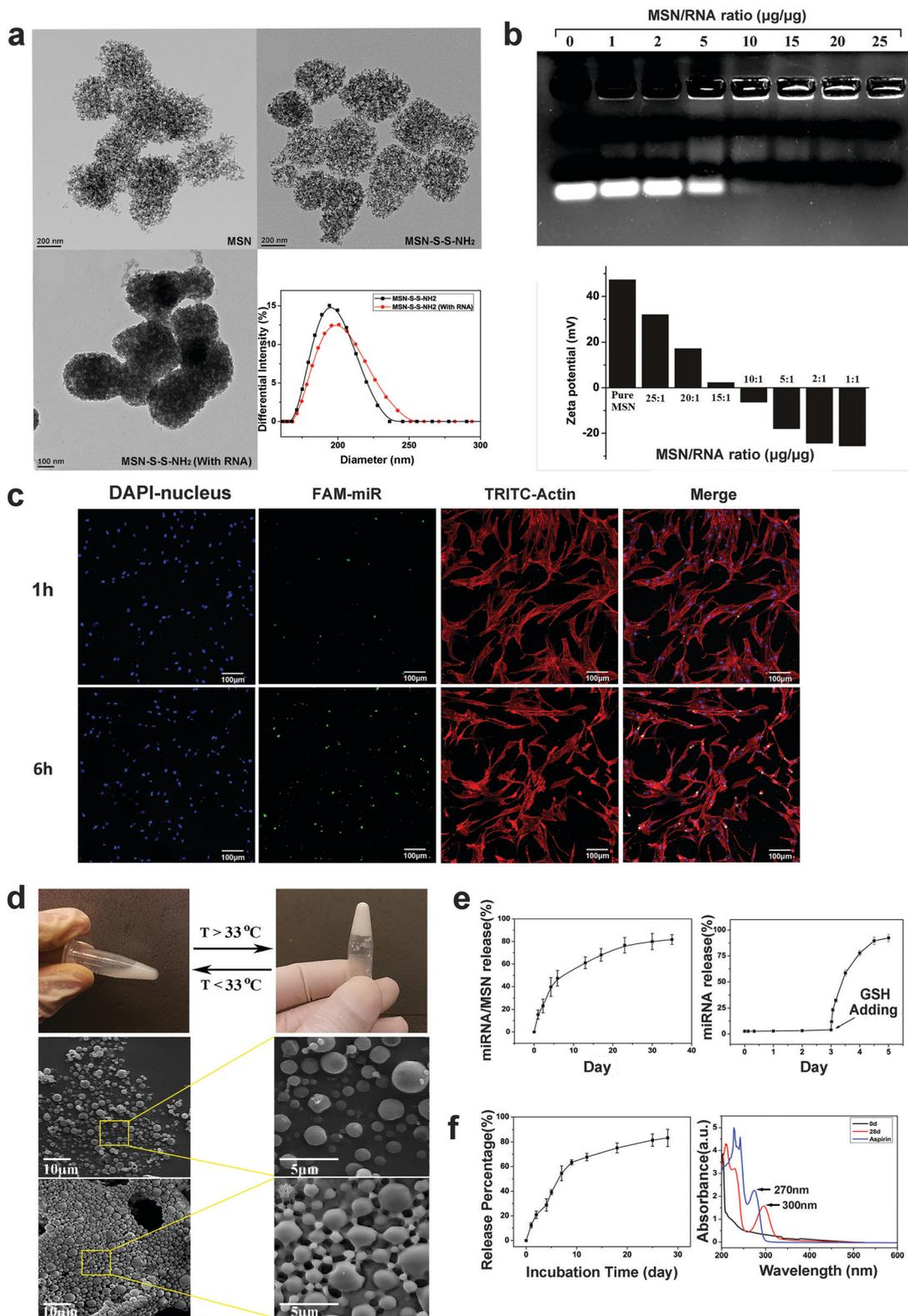
The MSNs designed for miR222 release (miR222/MSN) were developed, then, the functionalization and miR222 loading of MSNs were examined by transmission electron microscopy

(Fig. 3a). The MSNs had a porous and spherical morphology with a diameter of 200 nm, and no visible changes occurred after modification with disulfide bonds and amino groups. The pores were mostly filled after 30 min of miR222 absorption, demonstrating the miR222-loading capacity of the MSNs. Infrared spectra and δ potential measurements revealed the characteristic covalent bond vibrations of MSN, thiol, and amino groups (Fig. S1, ESI†) as well as the surface charges of MSNs according to the electrical properties of each functional component (Fig. S2, ESI†).

To quantify the miR222 loading capacity, we performed a gel retardation assay with complexes of miR222 (0.5 μg) and varying concentrations of MSN-S-S-NH$_2$ (0–12.5 μg). The results showed that a large amount of condensed miR222/MSN complex remained in the well with negligible release of miR222 when the ratio between MSN and miR222 was greater than 10 (Fig. 3b). The surface charge of MSN-S-S-NH$_2$ with and without different amounts of miR222 was also estimated by the zeta potential, which was about 47 mV in pH 7.4 buffered solution for MSN-S-S-NH$_2$.

As the charge of miRNA is negative, while the surface charge of MSNs is positive, so the zeta potential of miR222/MSN complexes gradually became negative with the increase amount of miR222 loading but remained positive until the MSN-to-miR222 ratio decreased to 15:1, that miR222/MSN complexes would bind with the negatively charged cell membranes to enhance the endocytosis, suggesting that the optimal loading capacity of miRNA is around 6.6 wt% (MSN:miR222 = 15:1). Subsequent experiments were performed with 6.6 wt% miR222/MSN complexes.

The intracellular release of miR222 from MSNs was investigated by confocal assay (Fig. 3c). The strong punctate green fluorescent signal corresponding to aggregated miR222/MSN

This journal is © The Royal Society of Chemistry 2019

J. Mater. Chem. B, 2019, **7**, 2722–2735 | **2725**

Fig. 3 (a) Transmission electron microscopy images of porous and spherical morphology of MSNs and miR222/MSNs. (b) Optimal loading capacity of miR222 for the system was 15 : 1 (MSN: miR222), determined by gel retardation assay and zeta potential measurement. (c) Cellular uptake of FAM-conjugated miR222 after 1 h and 6 h, as determined by confocal analysis. Green: miR222/MSN; red: F-actin; blue: cell nucleus. (d) Photographs of the thermal responsive microspheres-hydrogel transition, and the scanning electron microscopy images of corresponding microspheres in solution state and hydrogel state. (e) Release profile of miR222/MSN complexes for 35 days *in vitro* and GSH was required to trigger burst release of miR222. (f) Release profile of ASP for 28 days *in vitro* and the absorbance of ASP dissolved in supernatant at day 0 (black), day 28 (red), and the absorbance of ASP extracted from MSNs hygrogel (blue) ($n = 3$).

2726 | *J. Mater. Chem. B*, 2019, **7**, 2722–2735

This journal is © The Royal Society of Chemistry 2019

complexes was increased in the cytoplasm of BMSCs from 1 to 6 h post incubation, indicating efficient miR222 delivery by MSNs in the hydrogel.

Various vehicles are available for drug and gene delivery. Nanocarriers including liposomes, cationic polymers, and nanoparticles have been widely used.[37] Here we use MSNs (Fig. 3a) as a nanocarrier owing to its numerous advantages, which include their large superficial area, abundant pore size, well-demarcated pore structure, excellent biocompatibility, and a surface that is highly amenable to functionalization.[38] Besides, MSNs is an excellent category of materials ready to be used in clinic. As silica is "generally recognized as safe" by the Food and Drug Administration (FDA) in America, silica-based nanomaterials have been extensively investigated for drug delivery strategies for their non-toxic nature,[39] as they would slowly degrade to orthosilicic acid $(Si(OH)_4)$ which is easily carried by the blood or lymphatic system and subsequently excreted through the kidneys.[40,41] Functionalized MSNs have been used as a cargo delivery vehicle for drugs, DNA, and RNA and have shown efficient intracellular release.[42–44] However, after being endocytosed by cells, current MSN-based gene delivery vehicles mostly result in burst release of drugs that only lasts a few hours.[45,46] This is contrary to the requirement of prolonged miRNA transfection for the induction of neuronal differentiation to enhance bone formation. As such, we modified the MSNs with disulfide bonds and amino groups to bind with miR222, so as to stabilize miR222 outside of the cells. Stimuli-responsive MSNs is a variety of functional materials investigated for targeted drug delivery and cancer therapy. There are mainly several types of stimuli-responsive MSNs as redox-responsive, pH-responsive and light-responsive MSNs.[47–50] In our MSNs system, the disulfide bonds were sensitive to redox reaction with endogenous glutathione (GSH), when miR222/MSN is endocytosed by cells, disulfide bonds will break up by GSH and miR222 is released (Fig. 3e).

2.3 Formation of thermally responsive colloidal hydrogel by PEG–PLGA–PNIPAM, ASP and miR222/MSN

Aspirin has long been used as a non-steroidal anti-inflammatory drug for relieving pain, reducing inflammation and preventing cardiovascular diseases in clinic.[51,52] The bone healing process is an osteo-immunological event with inflammation involved. The initial stage of bone healing process is an acute inflammation stage, macrophages are recruited in this stage. By secreting inflammatory and chemotactic mediators, macrophages then start to recruit mesenchymal stem cells (MSCs) and osteoprogenitor cells and ultimately generate new bone.[53–55] However, macrophages can also regulate osteoclasts activity through secreting inflammatory cytokines such as tumor necrosis factor α (TNF-α), interferon γ (IFN-γ), interleukin 1 (IL-1) and interleukin 6 (IL-6)[56–58] that result in bone resorption. ASP has been shown to modulate the balance between bone resorption and formation in ovariectomized-induced osteoporosis.[59] Moreover, it could improve calvarial bone regeneration in C57BL/6 mice by suppressing TNF-α and IFN-γ in hBMSCs.[60] More importantly, a recent study focusing on ASP showed that it could promote

osteogenesis by inhibition of macrophage activation under inflammatory conditions.[22] With this consideration, aspirin was used in our study as an anti-inflammation drug to suppress inflammatory conditions and improve bone healing.

The synthesized PEG–PLGA–PNIPAM copolymer, commercially available ASP (Sigma, A2093, Darmstadt, Germany) and miR222/MSN complexes were used to fabricate the miR222/MSN and ASP co-embedded core–shell microspheres by a well-established double-emulsion method.[61] To test the thermal responsiveness of the formed hydrogel, ASP and miR222/MSN co-embedded microsphere solution (30 wt%) was incubated at 37 °C and 25 °C respectively for 5 min (Fig. 3d). At temperatures over 33 °C, a lower critical solution temperature (LCST) of PEG–PLGA–PNIPAM markedly increased the viscosity of the liquid to yield hydrogel, Incubation at room temperature (25 °C) restored the low-viscosity state; the structural changes were visualized by scanning electron microscope. Further dynamic light scattering revealed that the microspheres had an outer diameter of about 2 μm and retained spherical morphology at room temperature (Fig. S3, ESI†).

The transition from hydrogel to nanoparticle solution could be repeatedly induced at different temperatures, which was likely due to (1) the reversible change between stretched (below the lower critical solution temperature (LCST)) and constricted (above LCST) structures of PNIPAM chains on the surface of microspheres; and (2) the tangling of PNIPAM chains during their constriction. Though a recent study proved that MSNs could enhance the elastic moduli of alginate hydrogel,[62] further experiments need to be conducted to test the mechanical properties of this MSNs PEG–PLGA–PNIPAM hydrogel while keeping its injectability for intended applications.

The development of an effective RNA delivery system is a challenging task as RNA readily undergoes degradation, in addition, it is difficult to preserve their activity via prolonged release strategy. Our miR222/MSN/ASP microspheres self-assembled into a biodegradable hydrogel via temperature-induced hydrophobic interactions between PNIPAM chains immediately after injection (Fig. 3d), and underwent gradual degradation for sustained release of the payload (miR222/MSN complex) over a period of weeks. Pre-immobilization of the amino group of MSN via disulfide bonds provided loading sites for miR222 and GSH for cytoplasmic release (Fig. 3e). GSH, a tripeptide that is commonly distributed in mammalian cells, reacts with disulfide bonds (Pubchem). In this manner, the controllable delivery of miR222 was achieved in a two-stage reaction manner that enabled sustainable and effective transfection into cells.

2.4 Evaluation of miR222 and ASP release characteristics

The controlled release of miR222/MSN complexes from hydrogel and that of miR222 from MSNs was investigated under simulated physiological conditions of the extra- and intracellular environments, respectively. The release profile of miR222/MSN complexes over time was determined by monitoring the weight of miR222/MSN complexes in a given amount of solution after complete removal of the PEG–PLGA–PNIPAM copolymer via repeated washes with dimethylformamide. As is shown in Fig. 3e, an initial

This journal is © The Royal Society of Chemistry 2019

J. Mater. Chem. B, 2019, **7**, 2722–2735 | **2727**

burst release of 15% of miR222/MSN complexes on the first day and total release of 80% at the end of 35 days was observed. GSH was required to trigger miR222 release from MSNs; the percentage of miR222 released from MSNs after 3 days of incubation in phosphate-buffered saline (PBS) was less than 3%, owing to the desorption of a small quantity of miR222 from the MSN surface. However, in the presence of GSH, miR222 was dramatically released from the inside of MSN over time, reaching 90% over 2 days. These data demonstrate the controlled delivery of miR222 over a long period of time, and its selective release in the intracellular environment through loading on MSNs in a PEG–PLGA–PNIPAM microsphere-based hydrogel. The release profile of ASP from MSN/ASP hydrogel was monitored by ultraviolet-visible (UV) spectrophotometry by recording the absorbance at around 300 nm. The release profile of ASP was linear in the first 10 days, with about 60% of ASP appearing in the solution (Fig. 3f). Thereafter, the release rate declined and ASP release nearly reached its end at day 28, with an accumulated ASP percentage >80%, which is in accordance with the release profile of miR222/MSN. These results indicate that miR222 can be released in conjunction with ASP in a controlled fashion.

2.5 *In vivo* effects of miR222/MSN/ASP hydrogels

To investigate the capacity of miR222/MSN/ASP hydrogel for neurogenic induction during bone formation, we created a 5 mm diameter mandibular bone defect model in rats.[63,64] The animals were divided into MSN, MSN/ASP, and miR222/MSN/ASP hydrogel groups. Rat mandible bone tissue specimens were harvested after 10 weeks and overall bone formation was evaluated by micro-computed tomography (micro-CT). Histochemical staining of hematoxylin & eosin (H&E) and Masson's trichrome of paraffin-embedded tissue sections were also conducted.

The micro-CT scan revealed that newly generated mineralized tissue mainly grew from the bone defect margin to the center (Fig. 4a); a quantitative analysis showed that the new bone volume/total volume percentage (BV/TV%) was higher in the miR222/MSN/ASP group (21.97% ± 3.99%) than in the MSN (6.14% ± 1.47%), and MSN/ASP (11.93% ± 1.57%) groups ($P < 0.05$) (Fig. 4b). Comparison of MSN and MSN/ASP groups, revealed no significant difference in new bone formation, indicating that ASP alone could not promote osteogenesis in rat mandibular defect.

In the H&E-stained cross-sections of mandible tissue, no obvious inflammatory cells were observed (Fig. 4c). However, further immunohistochemistry staining is needed to detect any specific inflammatory cells, such as macrophages. Compared with the MSN and MSN/ASP groups, there was more newly formed bone tissue at the inner edge of the defect in the miR222/MSN/ASP group, which showed bone-like structures extending from the regenerated tissue in the middle of the defect area. In contrast, there was less new bone tissue generated in the MSN/ASP group and almost none in the MSN group. A large area of collagen extending from both sides of the defect zone was observed in the miR222/MSN/ASP group by Masson's trichrome staining, whereas in the MSN/ASP and MSN groups, there was relatively little collagen (Fig. 4d).
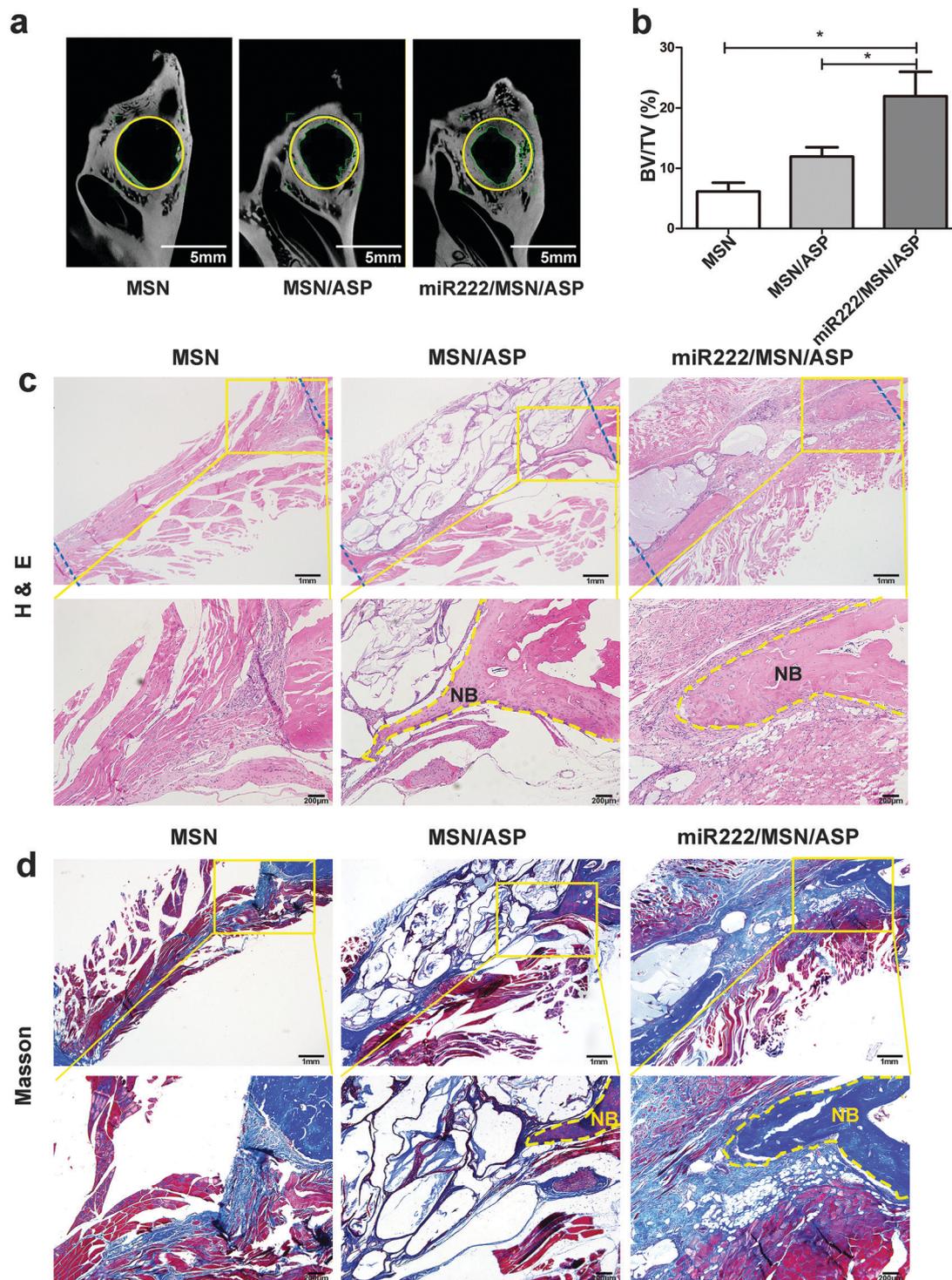
On the basis of the findings of our previous study and current studies of ASP,[20,65,66] the fact that little bone formation was observed in the MSN/ASP group (Fig. 4a) may be attributed to the absence of ASP pre-treated seed cells in the defect area. Referring to more recent studies, the *in vivo* osteogenic potential of ASP may be largely reliant on the osteoblastic differentiation ability of ASP-treated BMSCs seeded together with scaffolds *in vivo*. In the present study, only the miR222/MSN/ASP group showed generation of significantly more newly formed bone, as suggested by statistical analysis, showing that miR222 together with ASP stimulates bone regeneration. The possible mechanism would be therefore discussed later.

2.6 Detection of neurogenic marker expression

Fluorescent immunohistochemistry analysis of the neuronal protein Tuj1 and glial protein S100 were performed to reveal innervation in bone defects (Fig. 5a and b). Both markers were more highly expressed in the newly formed bone tissue of the miR222/MSN/ASP compared with that in the MSN/ASP group. A quantitative analysis of the average optical densities of Tuj1 and S100 showed significant increased expression of these neurogenic proteins in the miR222/MSN/ASP group (Fig. 5c). Given that more bone tissue was generated in the defect area of the miR222/MSN/ASP group compared with that in the MSN/ASP group, the results indicate that sustained release of miR222 can induce innervation in engineered bone tissue in with the presence of ASP.

In comparison with previous studies of integration of nerve tracts into bone scaffolds or magnesium implants to improve fracture healing,[6–8] the present work achieved innervated bone formation without secondary trauma, and our controllable delivery system provides a promising approach for biologically safe and effective bone engineering. The high expression of neuronal proteins surrounding newly formed bone indicated innervation in the defect site. It is known that nerve fibers and vessels are coupled throughout whole bone and have a synergistic effect on bone growth. Nerve fibers secrete vasculogenic neuropeptides that can improve angiogenesis, while blood vessels contribute to nerve growth by providing oxygen and nutrients. As such, the present study of innervated bone engineering indicates promise for the achievement of biomimetic neurovascularized bone.

To further explain the higher degree of bone tissue generation in the better innervated miR222/MSN/ASP group in the defect area, we conducted an immunohistochemistry assay in both MSN/ASP and miR222/MSN/ASP groups to detect calcitonin gene related peptide (CGRP) (Fig. S4, ESI†). CGRP is a neuropeptide produced in peripheral and central neurons, which has been used as an indicator for nerve fibers in previous studies.[67] In addition, CGRP is reported to regulate bone formation that may attribute to WNT signaling pathway.[8,68–70] Remarkably, fact that CGRP was clearly observed around the newly generated bone in the miR222/MSN/ASP group but not in the MSN/ASP group. This finding indicates the following underlying mechanism: at first, miR222 enhanced the neurogenic differentiation of BMSCs from the defect area, and BMSCs underwent differentiation

2728 | *J. Mater. Chem. B*, 2019, **7**, 2722–2735

This journal is © The Royal Society of Chemistry 2019

Fig. 4 (a) Micro-CT scan of bone in the mandibular defect areas of rats in the MSN, MSN/ASP, and miR222/MSN/ASP microsphere hydrogel groups. (b) Statistical analysis of differences in BV/TV % between groups, miR222/MSN/ASP showed significant more new bone formation. (c) H&E staining of more newly formed bone tissue from the inner edge of the old bone in the miR222/MSN/ASP group, whereas MSN and MSN/ASP group had less bone-like tissue. (d) Masson's trichrome staining of more collagen (blue) in the defect zone in miR222/MSN/ASP group comparing with MSN and MSN/ASP group; *$P < 0.05$ ($n = 3$).

into neural-like cells and secreted CGRP to promote osteogenic differentiation in nearby BMSCs. ASP then further increased the osteogenic potential in CGRP-stimulated BMSCs near neural-like cells, thus achieving accelerated bone regeneration with better innervation. However, this is merely an assumption based on the existing results; further animal experiments and
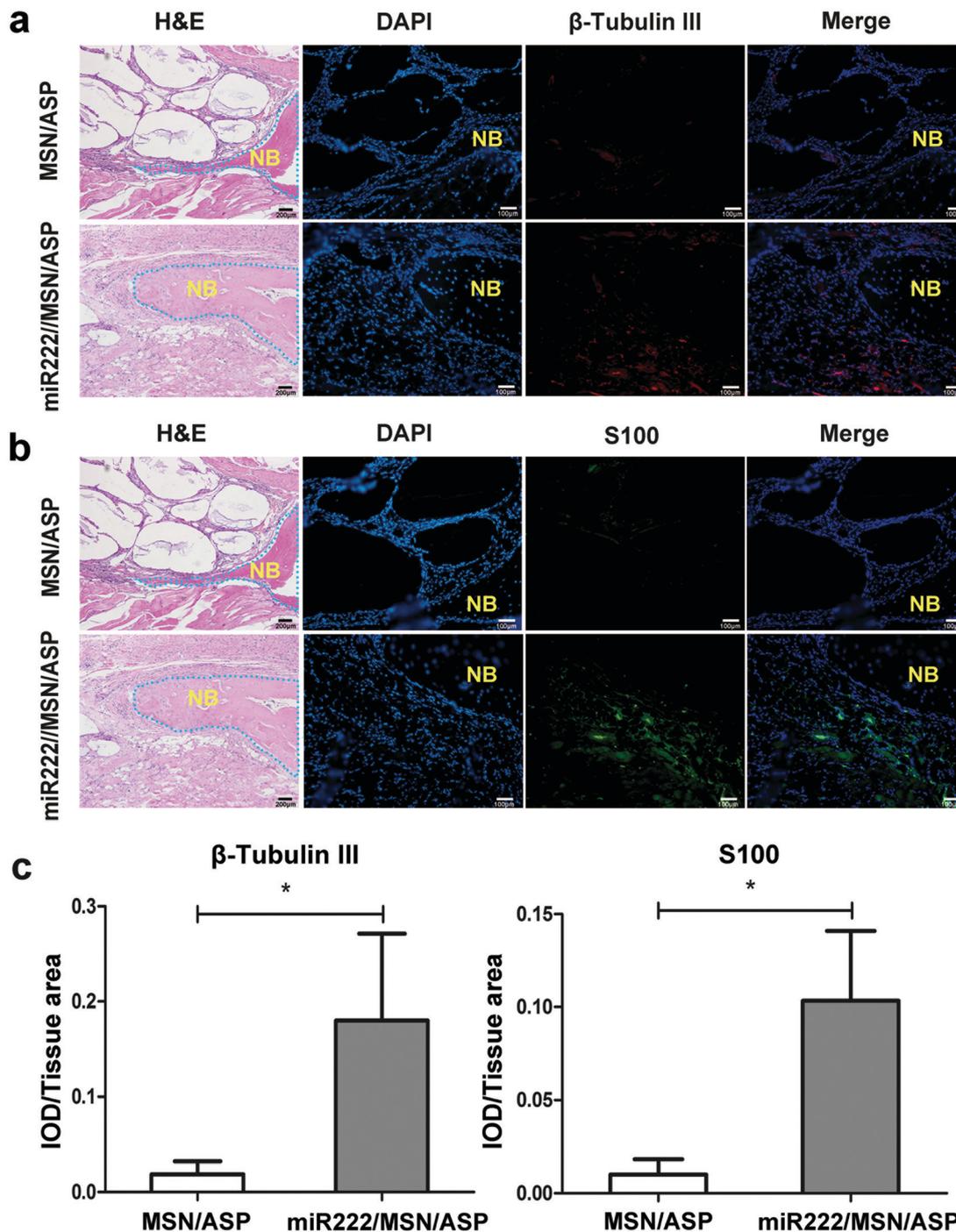
This journal is © The Royal Society of Chemistry 2019

J. Mater. Chem. B, 2019, 7, 2722–2735 | 2729

Fig. 5 (a and b) Expression of neuronal proteins Tuj1 and S100 in the MSN/ASP, and miR222/MSN/ASP microsphere hydrogel groups. The proteins were distributed around the newly formed bone tissue in the miR222/MSN/ASP group, whereas less protein was detected in MSN/ASP group. NB: new bone. (c) Statistical analysis of average optical density of Tuj1 and S100 showed significant differences; *$P < 0.05$ ($n = 3$).

studies involving the application of CGRP receptor blockers, and gene-deficient mice are necessary to confirm this hypothesis.

Bone defect of 5 mm in diameter in rats is the critical bone defect size, *i.e.*, it will not union under natural conditions,[71] and full regeneration was not achieved in the animal experiments. To avoid side effects of exogenous cells transplantation, stem cells were not applied in the animal experiments, though

previous study demonstrated stem cells pre-treated with ASP would fully generate calvarial defects.[20] In this study, injectable MSNs hydrogel loaded with drugs were mainly for forming innervated new bone. In the following studies, we will attempt to achieve full generation of innervated functional bone tissue with minimum secondary injury, probably by combining the commercialized calcium phosphate material while keep its

injectability through decreasing the particle size of calcium phosphate to nanoscale.

3. Conclusions

In summary, miR222 was confirmed *in vitro* to induce neural differentiation in hBMSCs, with potential utility for engineering innervated bone. We additionally developed an injectable, thermoresponsive miR222/MSN/ASP hydrogel for sustained miR222/ASP co-delivery to effectively induce innervated bone formation. Our *in vivo* results showed that this miR222/MSN/ASP hydrogel can stimulate bone regeneration with high expression of neural-related proteins. The results imply that the miR222/MSN/ASP hydrogel is capable of creating a microenvironment that promotes neurogenesis and bone regeneration, with potential applications for the formation of new biomimetic innervated bone tissue.

4. Experimental

4.1 hBMSC culture

hBMSCs were collected from healthy spongy bone removed during orthognathic surgeries at the Peking University Hospital of Stomatology with patient consent and approval of the Board of Peking University School of Stomatology (PKUSSIRB-201520020). Cells were collected and isolated according to our previous studies[9,23] and cultured in 10 cm culture dishes in proliferation medium (PM), which is α-Minimal Essential Medium (α-MEM) with 10% (v/v) fetal bovine serum (FBS) (#10099-141, Gibco, NY, USA), 1% (v/v) amphotericin B, penicillin, and streptomycin (#15240112, Gibco, NY, USA), in a CO_2 incubator at 37 °C. The ability of hBMSCs to undergo osteogenic differentiation was evaluated by alkaline phosphatase (ALP) and alizarin red staining, and the adipogenic differentiation potential was confirmed by oil Red O staining. The hBMSCs were passaged when the confluence reached 80%, and cells from passages 4 to 8 were used for experiments.

4.2 *In vitro* cell transfection and neural induction

hBMSC were seeded at a density of $3.0–5.0 \times 10^5$ cells per well on 6-well culture plates and cultured overnight in PM. For miR222 transfection, 5 μL of 50 nmol L^{-1} miR222 NC (microON miRNA mimic control), miR222 mimic[72] (microON miRNA mimic), or miR222 inhibitor (microOFF miRNA inhibitor) (all from RiboBio, Guangzhou, China) were separately mixed with 10 μL of Lipofectamine 2000 reagent (Invitrogen, CA, USA), and the three mixtures were added to separated wells; 24 h after miR222 transfection, the two-stage neural differentiation procedure was carried out over 12 days as previously described.[73,74] The medium was changed to pre-induction medium, which is Dulbecco's Modified Eagle Medium/Nutrient Mixture F-12 (DMEM/F12) with 2% (v/v) B-27 serum-free supplement (Gibco), 20 ng mL^{-1} epidermal growth factor (EGF; PeproTech) and 20 ng mL^{-1} basic fibroblast growth factor (bFGF; PeproTech). The pre-induction medium was changed every two days After 7 days,

the medium was changed to induction medium with DMEM/F12 containing 10% FBS, 2% B-27 serum-free supplement, 10 ng mL^{-1} EGF, and 10 ng mL^{-1} bFGF, after which the cells were collected for analysis.

4.3 Quantitative (q)RT-PCR

After transfection with miR222 and induction of neural differentiation for 12 days, hBMSCs were collected. Then, RNA was extracted using TRIzol (Invitrogen) and quantified by spectrophotometry. Reverse transcription was performed with 2 μg RNA using the cDNA Synthesis kit (ThermoFisher Scientific, USA). qRT-PCR was performed on an ABI PRISM 7500 System (Applied Biosystems, USA). The reaction volume was 10 μL per tube, which included 1 μL of cDNA, 1 μL of primers mixtures, 3 μL Milli-Q, and 5 μL SYBR Green mix (Roche Diagnostics, Mannheim, Germany). Glyceraldehyde 3-phosphate dehydrogenase (GAPDH) was used as the endogenous reference gene. MAP2, NGF, NG2, NLK and β-catenin were detected using the following forward and reverse primer sets (5′ to 3′ directions): GAPDH, ACAACTTTGGTATCGTGGAAGG and GCCATCACGCCACAGTTTC; MAP2, ACCCTCTTCATCCTCCCTGT and ACCTCACTGGACCTCAGCAC; NGF, CATCATCCCATCCCATCTTC and CTCTCCCAACACCATCACCT; NG2, CACGGCTCTGACCGACATAG and CCCAGCCCTCTACGACAGT; NLK, CCAACCTCCACACATT GACTATT and ACTTTGACATGATCTGAGCTGAG; β-catenin CAT CTACACAGTTTGATGCTGCT and GCAGTTTTGTCAGTTCAGGGA. Relative expression levels of target genes were determined using the ΔΔCt method.[75]

4.4 Western blotting

The transfected hBMSCs that had undergone neural induction were lysed in RIPA lysis buffer (Solarbio, Beijing, China) with 2 min of discontinuous ultrasonication on ice, then centrifuged with a speed at $12\,000 \times g$ (5418 R, Eppendorf, Germany) at 4 °C. Sodium dodecyl sulfate–polyacrylamide gel electrophoresis was performed to separate proteins by their molecular weights using a total of 20 μg 20 μL protein per lane. The protein bands were then transferred to a polyvinylidene difluoride membrane (Millipore, Billerica, MA, USA) which was blocked in 5% nonfat milk for 1 h (Huaxingbio Biotechnology, Beijing, China) containing 0.1% Tween-20 (Solarbio) before overnight incubation at 4 °C with antibodies against the following proteins: GFAP (1 : 2000, ab33922), NG2 (1 : 1000, ab139406), and Tuj1 (1 : 2000, ab78078) (all from Abcam, Cambridge, UK); NLK (1 : 1000, abs100383; Absin, Shanghai, China); β-catenin (1 : 1000, #8480; CST, USA); and GAPDH (1 : 1000, TA-08; ZSGB-Bio, Beijing, China). Horseradish peroxidase-conjugated anti-rabbit or -mouse IgG (1 : 10 000; ZSGB-Bio) was applied at room temperature (25 °C) for 1 h as appropriate for primary antibody detection. Protein bands were visualized by chemiluminescence (Solarbio) using an analyzer (Fusion FX5; Vilber, France). Quantification of protein bands was statistically analyzed using Image J (NIH).

4.5 *In vitro* immunofluorescence labeling of hBMSCs

Cells seeded on slides were fixed with 4% (v/v) paraformaldehyde (BSCX-Biotech, Beijing, China) and washed three times with PBS

This journal is © The Royal Society of Chemistry 2019

J. Mater. Chem. B, 2019, **7**, 2722–2735 | 2731

for 3 min. Then, 0.1% (v/v) Triton X-100 was used to permeabilize cells. Next, cells were blocked with 5% (w/v) bovine serum albumin and incubated overnight at 4 °C with antibodies NG2 (1 : 250, sc-53389; Santa Cruz, USA) and GFAP (1 : 500) separately. Samples were then incubated with respective secondary antibodies as fluorescein-conjugated goat anti-mouse IgG (1 : 50, ZF-0312) and anti-rabbit IgG (1 : 50, ZF-0311) (both from ZSGB-Bio) at room temperature for 1 h in dark, mounted with 4′,6-diamidino-2-phenylindole medium (DAPI) (ZSGB-Bio; ZLI-9557), and imaged using an IX71 microscope (Olympus, Japan).

4.6 Luciferase reporter assay

293T cells (ATCC® CRL-11268, USA) (3×10^5 per well) were seeded in DMEM with 10% FBS and transfected when they reached 80% confluence. The pEZX-MT05 reporter plasmid (GeneCopoeia, Rockville, MD, USA) containing wildtype (WT) and mutant (MUT) miR222 binding sites in the 3′ untranslated region of the NLK gene was used to generate reporter constructs, with the latter serving as a NC. miR222 mimic or NC was co-transfected with the reporter plasmids using Lipofectamine 2000; the four groups were miR-NC + WT, miR222 mimic + WT, miR-NC+ MUT, and miR222 mimic + MUT. Gaussia luciferase activity (GLuc) and secreted alkaline phosphatase (SEAP) luciferase activity in culture medium were measured 20 h later using the Dual Luminescence Assay kit (GeneCopoeia). SEAP luciferase activity was measured as an internal reference for normalization.

4.7 Synthesis and modification of MSNs for miR222 delivery

As previously described,[39,76,77] 1.12 g cetyltriethylammnonium bromide (CTAB) was dissolved in 1000 mL deionized water. With magnetic stirring, 52.8 mL ammonium hydroxide (29 wt% NH_3 in water) was added to approximately adjust the pH value to 11. Then 5.8 mL tetraethyl orthosilicate (TEOS) were added with rapid stirring and the resulting solution was heated up to 50 °C for 2 h. After being aged overnight, the mixture was centrifuged and precipitation was collected and washed thoroughly with distilled water and ethanol for three times respectively. Then the product was dispersed in acidic methanol (9 mL of HCl/400 mL of methanol) for 36 h at 70 °C to remove the surfactant templates. After being further centrifuged and washed with ethanol, as-synthesized MSNs were got from vacuum drying method for 20 h.

The as-synthesized MSNs were dispersed in 50 mL anhydrous ethanol, and added with 1 mL of 50% (in ethanol) 3-(trimethoxy-silyl) propyl methacrylate. After being stirred for 8 h, the resultant solid was filtered, and washed with ethanol. Thiol-MSN was obtained from vacuum drying method.

To prepare thermoresponsive MSNs for miR222 delivery, the purified thiol-MSN (1.00 g) was treated with a methanol solution (60 mL) of 2-(pyridyldisulfanyl) ethylamine (PDEA) (9.12×10^{-4} mol) at room temperature for 24 h under vigorous stirring to undergo the desired disulfide bond exchange reaction. The resulting amino groups functionalized mesoporous silica nanosphere through disulfide linkage ($MSN-S-S-NH_2$) were filtered and washed with methanol and dried in air (Scheme 1a).

4.8 Gel retardation assay

For the gel retardation assay, $1\times$ Tris base–acetic acid–ethylene-diaminetetraacetic acid (EDTA) buffer containing 1% (w/v) agarose gel and $1\times$ Goldview nuclear stain (G8142; Solarbio) were used. Complexes of miR222 (0.5 µg) and varying concentrations of $MSN-S-S-NH_2$ (0–12.5 µg) along with $10\times$ loading buffer were added to the wells and the samples were resolved at 100 V for 10 min. The gel was visualized with an image analyzer.

4.9 Cellular uptake assay

hBMSCs were seeded and cultured on coverslips in 24-well plates in PM. miR222/MSN microspheres were labelled by FAM-conjugated miR222. hBMSC cells were co-cultured with FAM-conjugated miR222/MSN microspheres and fixed with 4% (v/v) paraformaldehyde (BSCX-Biotech) after incubation for 1 h or 6 h. Cells were permeabilized with 0.1% (v/v) TritonX-100; then, the cytoskeleton was stained with TRITC labelled-phalloidin (1 : 200; Solarbio) before mounting with DAPI. Samples were imaged with a laser confocal microscope (Leica, Germany).

4.10 Preparation of miR222/MSN/ASP-embedded microsphere

The PEG–PLGA–PNIPAM copolymer was fabricated by atom transfer radical polymerization and ring opening co-polymerization, based on a previous study[78,79] with modifications. PEG–PLA copolymer was synthesized with cyclic dimers (1,4-dioxane-2,5-diones) of glycolic and lactic acids through ring-opening co-polymerization, using methoxy polyethylene glycol as the initiator and $Sn(Oct)_2$ as the catalyst. A haloid tail was added to PEG–PLGA to generate PEG–PLGA–Br, which was used as a macroinitiator for final atom transfer in the radical polymerization with N-isopropylacrylamide. The synthesized PEG–PLGA–PNIPAM copolymer, miR222/MSN complexes (MSN : miR222 = 15 : 1) and ASP were used to fabricate miR222/MSN/ASP-embedded core–shell microspheres via a double-emulsion method.[80] In this process, a water phase consisting of miR222/MSN complexes (W1), a dichloromethane phase consisting of PEG–PLGA–PNIPAM copolymer and ASP (O), and another water phase consisting of polyvinyl alcohol (PVA) (W2) were reacted and the W1/O/W2 emulsion were synthesized referring to the published literature.[81] In this system, W1 phase comprised 30 mg miR222/MSNs complexes dissolved in 100 µL PBS; 40 mg PEG–PLGA–PNIPAM copolymer together with 20 mg ASP were dispersed in 1 mL dichloromethane as the O phase; W2 phase was 10 mL of 1% (w/v) PVA. Next, the droplets were solidified to form the miR222/MSN/ASP-embedded core–shell microspheres via ultrasonication.

4.11 In vitro release assay of miR222/MSN complexes and miR222

Prior to the release experiment, the sample was washed three times with PBS buffer to remove the unloaded drugs. The initial incorporated amount of miRNA/MSN complexes in the hydro-gel was defined by the weight of solid residue after complete

2732 | J. Mater. Chem. B, 2019, 7, 2722–2735

This journal is © The Royal Society of Chemistry 2019

removal of the PEG–PLGA–PNIPAM copolymer form the hydrogel *via* repeated DMF wash. The release percentage of miRNA/MSN complexes and miRNA were calculated based on setting the initial incorporated amount as 100%. The release profiles of miR222/MSN complexes from the colloidal hydrogel were tested in PBS buffer. The hydrogel was soaked in 200 μL PBS and placed in a shaker at a temperature of 37 °C and speed of 50 rpm. The release solution was collected at day 0, 2, 4, 6, 8, 14, 18, 24, 30 and 35 and replaced with newly prepared PBS. The collected solution was then centrifuged at $15\,000 \times g$ (5418 R, Eppendorf, Germany) for 20 min. The weight of resulted precipitate was measured after complete removal of the PEG–PLGA–PNIPAM copolymer *via* repeated *N,N*-dimethylformamide (DMF) washing, to determine the released amounts of miR222/MSN complexes.

The stimuli-responsive release of miR222 from the MSN vehicles was examined by incubating the miR222/MSN complexes released from the hydrogel in PBS buffer with or without GSH ((i) day 0–3, PBS in the absence of GSH, (ii) day 3–5, PBS in the presence of GSH). The initial incorporated amount of miRNA in MSNs was calculated by the concentration change of miRNA solution before and after MSNs encapsulation. After being centrifuged at $15\,000 \times g$ (5418 R, Eppendorf, Germany) for 20 min, 2 mL of supernatant was collected at each time. Then with 5 min of incubation at room temperature with QuantiFluor RNA Dye working solution, the release amount of miR222 from the MSN vehicles was examined using a ThermoElectron 3001 Scanning Microplate Reader.

4.12 *In vitro* release assay of aspirin

Prior to the release experiment, the sample was washed three times with PBS buffer to remove the unloaded ASP. To define the initial incorporated amount of aspirin in the hydrogel, the hydrogel was firstly dissolved in chloroform. Then the supernatant was collected and measured by UV-Vis spectra at 300 nm to determine the amount of aspirin. The release percentage of aspirin is calculated based on setting the initial incorporated amount as 100%. *In vitro* release profiles of aspirin from the colloidal hydrogel were determined as follows. Hydrogel formed by 30 mg of miR222/MSN/ASP-embedded core–shell microspheres were soaked in 3 mL of PBS and shaken at 60 rpm (37 °C). Then, 1 mL of release solution was collected and replaced with fresh PBS each time. The collected release media were then centrifuged and the supernatant was measured by UV-Vis spectra at 300 nm to determine the release amount of aspirin.

As for the absorbance of aspirin, aspirin encapsulated in PEG–PLGA–PNIPAM copolymer was firstly extracted with water, and the absorbance was measured as 270 nm (Fig. 3f, blue line), which is in accordance with the absorbance of pure aspirin, indicating aspirin was chemically stable in PEG–PLGA–PNIPAM copolymer. While in the *in vitro* release assay, after being dissolved in water for over 12 h, the absorbance of aspirin turned to 300 nm which was actually the absorbance of salicylic acid, product of aspirin hydrolysis (Fig. 3f, black line for 0 day; red line for 28 day).

4.13 Rat mandibular defect model and hydrogel injection

Animal procedures were approved by the Biomedical Ethical Committee of Peking University (LA2015158). Nine male Sprague-Dawley rats weighing 160–180 g were used to generate mandibular defect models. The rats were randomly divided into three groups according to the injected hydrogel material: MSN, MSN/ASP, and miR222/MSN/ASP (*n* = 3 each). Animals were anesthetized with 1% pentobarbital sodium and the mandible angle region on both sides was shaved and disinfected. Bilateral mucoperiosteal flaps were lifted and retracted. A round, penetrating critical size defect with a diameter of 5 mm was created on the mandible angle using a trephine burr. About 5 mg of material in 10 μL PBS were injected per site and straticulate saturation were conducted. Rats were monitored daily and no adverse effects were observed. Animals were sacrificed using carbon dioxide for euthanasia after 10 weeks and mandible samples were obtained and fixed in 10% neutral formalin liquid.

4.14 Micro-CT analysis

Rat mandible tissue samples were scanned by micro-CT (Munich, Germany) at current of 500 μA and a voltage of 80 kV, and the exposure time was 500 ms. A cylindrical region of interest was created (5 mm in diameter and 2 mm in height) in the mandibular defect area and designated as the region of interest. To distinguish new bone from soft tissue, the grayscale threshold is 1024.9, *i.e.* new bone tissue was designated as tissue area with grayscale above 1024.9 to the maximum, and below 1024.9 is soft tissue. All of our samples were analyzed with this threshold. Data were analyzed with Inveon Research Workplace v.4.2 software (Siemens). The percentage of bone volume (BV)/total volume (TV) was determined for each sample, and new bone volume was compared across groups.

4.15 Histological and immunofluorescence analyses

Mandible specimens were decalcified in 20% EDTA (pH = 7.2) for 8 weeks and then cut in half to obtain a cross section of the defect area. The tissue was embedded in wax. Then, 4 μm sections were cut using a microtome (Leica, Germany) and stained with H&E and Masson's trichrome using commercial kits (Solarbio) to assess bone formation.

Immunofluorescence detection of neural markers in the MSN/ASP and miR222/MSN/ASP groups was performed using primary antibodies against Tuj1 (1:200) and S100 (1:100, ab52642; Abcam) at 4 °C overnight; the samples were then incubated with respective secondary antibodies rhodamine-conjugated goat anti-mouse IgG (1:50, ZF-0313) and fluorescein isothiocyanate-conjugated goat anti-rabbit IgG (1:50, ZF-0311) (both from ZSGB-Bio) in the dark for 1 h. Samples were then mounted with DAPI and imaged with a fluorescence microscope. Three randomly selected fields from three slides in each sample were semiquantitatively assessed for the optical density of positive staining (integrated optical density/tissue area) by Image Pro Plus software (Media Cybernetics; Roper Technologies, Lakewood Ranch, FL).

This journal is © The Royal Society of Chemistry 2019

J. Mater. Chem. B, 2019, **7**, 2722–2735 | **2733**

4.16 Data analysis

Data analysis was carried out using SPSS v.13.0 software (IBM, NY, USA). Homogeneity of variance was checked as equal. The data were analyzed by one-way analysis of variance (ANOVA). Error bars represented standard deviation. Statistical significance level was set at $*P < 0.05$.

Conflicts of interest

There are no conflicts of interest to declare.

Acknowledgements

References

1 C. M. Serre, D. Farlay, P. D. Delmas and C. Chenu, *Bone*, 1999, **25**, 623.
2 A. Ramnemark, L. Nyberg, R. Lorentzon, U. Englund and Y. Gustafson, *Osteoporosis Int.*, 1999, **9**, 269.
3 U. H. Lerner, *J. Musculoskeletal Neuronal Interact.*, 2002, **2**, 440–447.
4 C. Chenu, *J. Musculoskeletal Neuronal Interact.*, 2004, **4**, 132.
5 A. Marrella, T. Y. Lee, D. H. Lee, S. Karuthedom, D. Syla, A. Chawla, A. Khademhosseini and H. L. Jang, *Mater. Today*, 2018, **21**, 362.
6 Y. Wu, D. Jing, H. Ouyang, L. Li, M. Zhai, Y. Li, L. Bi and G. Pei, *Tissue Eng., Part A*, 2015, **21**, 2241.
7 J. Fan, L. Bi, D. Jin, K. Wei, B. Chen, Z. Zhang and G. Pei, *BioMed Res. Int.*, 2014, 281872.
8 Y. Zhang, J. Xu, Y. C. Ruan, M. K. Yu, M. O'Laughlin, H. Wise, D. Chen, L. Tian, D. Shi, J. Wang, S. Chen, J. Q. Feng, D. H. Chow, X. Xie, L. Zheng, L. Huang, S. Huang, K. Leung, N. Lu, L. Zhao, H. Li, D. Zhao, X. Guo, K. Chan, F. Witte, H. C. Chan, Y. Zheng and L. Qin, *Nat. Med.*, 2016, **22**, 1160.
9 Q. Liu, L. Lei, T. Yu, T. Jiang and Y. Kang, *Tissue Eng., Part A*, 2018, **24**, 1283.
10 X. Gu, F. Ding and D. F. Williams, *Biomaterials*, 2014, **35**, 6143.
11 P. Koria, *BioDrugs*, 2012, **26**, 163.
12 N. F. Loohuis, A. Kos, G. J. Martens, H. Van Bokhoven, N. Nadif Kasri and A. Aschrafi, *Cell. Mol. Life Sci.*, 2012, **69**, 89.
13 S. Zhou, D. Shen, Y. Wang, L. Gong, X. Tang, B. Yu, X. Gu and F. Ding, *PLoS One*, 2012, **7**, e44768.
14 B. Yu, S. Zhou, Y. Wang, T. Qian, G. Ding, F. Ding and X. Gu, *J. Cell Sci.*, 2012, **125**, 2675.
15 P. J. Goadsby, R. B. Lipton and M. D. Ferrari, *N. Engl. J. Med.*, 2002, **346**, 257.
16 C. A. Trialists, C. Baigent, L. Blackwell, R. Collins, J. Emberson, J. Godwin, R. Peto, J. Buring, C. Hennekens,

P. Kearney, T. Meade, C. Patrono, M. C. Roncaglioni and A. Zanchetti, *Lancet*, 2009, **373**, 1849.
17 M. J. Thun, M. M. Namboodiri, E. E. Calle, W. D. Flanders and C. W. Heath, *Cancer Res.*, 1993, **53**, 1322.
18 F. A. Rahman, J. M. Ali, M. Abdullah, N. H. A. Kasim and S. Musa, *J. Periodontol.*, 2016, **87**, 837.
19 J. Zhang, S. Ma, Z. Liu, H. Geng, X. Lu, X. Zhang, H. Li, C. Gao, X. Zhang and P. Gao, *Int. J. Nanomed.*, 2017, **12**, 8855.
20 Y. Cao, J. Xiong, S. Mei, F. Wang, Z. Zhao, S. Wang and Y. Liu, *Stem Cell Res. Ther.*, 2015, **6**, 210.
21 J. Tang, J. Xiong, T. Wu, Z. Tang, G. Ding, C. Zhang, S. Wang and Y. Liu, *Stem Cells Dev.*, 2014, **23**, 2093.
22 Y. Liu, S. Fang, X. Li, J. Feng, J. Du, L. Guo, Y. Su, J. Zhou, G. Ding, Y. Bai, S. Wang, H. Wang and Y. Liu, *Sci. Rep.*, 2017, **7**, 11549.
23 T. Yu, Q. Liu, T. Jiang, X. Wang, Y. Yang and Y. Kang, *Adv. Funct. Mater.*, 2016, **26**, 6719.
24 K. M. Cadigan and M. L. Waterman, *Cold Spring Harbor Perspect. Biol.*, 2012, **4**, a007906.
25 K. C. Masoumi, R. Daams, W. Sime, V. Siino, H. Ke, F. Levander and R. Massoumi, *Mol. Biol. Cell*, 2017, **28**, 346.
26 H. Clevers, *Cell*, 2006, **127**, 469.
27 E. M. Toledo, M. Colombres and N. C. Inestrosa, *Prog. Neurobiol.*, 2008, **86**, 281.
28 S. T. Lee, K. Chu, W. S. Im, H. J. Yoon, J. Y. Im, J. E. Park, K. H. Park, K. H. Jung, S. K. Lee, M. Kim and J. K. Roh, *Exp. Neurol.*, 2011, **227**, 172.
29 A. Pandey, P. Singh, A. Jauhari, T. Singh, F. Khan, A. B. Pant, D. Parmar and S. Yadav, *J. Neurochem.*, 2015, **133**, 640.
30 X. Wang, Y. Xu, H. Zhu, C. Ma, X. Dai and C. Qin, *Mol. Med. Rep.*, 2015, **12**, 7687–7692.
31 J. Song, X. Li, Y. Li, J. Che, X. Li, X. Zhao, Y. Chen, X. Zheng and W. Yuan, *Int. J. Nanomed.*, 2017, **12**, 4195–4208.
32 M. Mariani, R. Karki, M. Spennato, D. Pandya, S. He, M. Andreoli, P. Fiedler and C. Ferlini, *Gene*, 2015, **563**, 109.
33 C. He, C. Liao and C. Pan, *Open Biol.*, 2018, **8**, 180116.
34 S. Jiao, Y. Liu, Y. Yao and J. Teng, *Mol. Cell. Biochem.*, 2018, **449**, 305.
35 E. N. Quiroz, R. N. Quiroz, M. Ahmad, L. G. Escorcia, J. L. Villarreal, C. F. Ponce and G. A. Martinez, *Cells*, 2018, **7**, 75.
36 M. Katoh and M. Katoh, *Clin. Cancer Res.*, 2007, **13**, 4042.
37 H. Wang, Y. Jiang, H. Peng, Y. Chen, P. Zhu and Y. Huang, *Adv. Drug Delivery Rev.*, 2015, **81**, 142.
38 Y. Zhao, J. L. Vivero-Escoto, I. I. Slowing, B. G. Trewyn and V. S. Lin, *Expert Opin. Drug Delivery*, 2010, **7**, 1013.
39 P. Kumar, P. Tambe, K. M. Paknikar and V. Gajbhiye, *J. Controlled Release*, 2018, **287**, 35–57.
40 P. Kortesuo, M. Ahola, S. Karlsson, I. Kangasniemi, J. Kiesvaara and A. Yli-Urpo, *J. Biomed. Mater. Res.*, 1999, **44**, 162–167.
41 P. Kortesuo, M. Ahola, M. Kangas, A. Yli-Urpo, J. Kiesvaara and M. Marvola, *Int. J. Pharm.*, 2001, **221**, 107–114.
42 X. Chen, X. Cheng, A. H. Soeriyadi, S. M. Sagnella, X. Lu, J. A. Scott, S. B. Lowe, M. Kavallaris and J. J. Gooding, *Biomater. Sci.*, 2014, **2**, 121.

43 X. Chen, A. H. Soeriyadi, X. Lu, S. M. Sagnella, M. Kavallaris and J. J. Gooding, *Adv. Funct. Mater.*, 2014, **24**, 6999.

44 Z. Liu, X. Chen, X. Zhang, J. J. Gooding and Y. Zhou, *Adv. Healthc. Mater.*, 2016, **5**, 1401.

45 K. Möller, K. Müller, H. Engelke, C. Bräuchle, E. Wagner and T. Bein, *Nanoscale*, 2016, **8**, 4007.

46 J. Lin, Z. Liu, Q. Zhu, X. Rong, C. Liang, J. Wang, D. Ma, J. Sun and G. Wang, *Colloids Surf., B*, 2017, **155**, 41.

47 L. Chen, X. Zhou, W. Nie, Q. Zhang, W. Wang, Y. Zhang and C. He, *ACS Appl. Mater. Interfaces*, 2016, **8**, 33829–33841.

48 M. Martínez-Carmona, D. Lozano, M. Colilla and M. Vallet-Regí, *Acta Biomater.*, 2018, **65**, 393–404.

49 Q. Lei, W. Qiu, J. Hu, P. Cao, C. Zhu, H. Cheng and X. Zhang, *Small*, 2016, **12**, 4286–4298.

50 J. Wen, K. Yang, F. Liu, H. Li, Y. Xu and S. Sun, *Chem. Soc. Rev.*, 2017, **46**, 6024–6045.

51 Y. Saito, S. Okada, H. Ogawa, H. Soejima, M. Sakuma, M. Nakayama, N. Doi, H. Jinnouchi, M. Waki, I. Masuda, T. Morimoto and JPAD Trial Investigators, *Circulation*, 2017, **135**, 659–670.

52 M. J. R. Desborough and D. M. Keeling, *Br. J. Haematol.*, 2017, **177**, 674–683.

53 Z. Xing, C. Lu, D. Hu, Y. Y. Yu, X. Wang, C. Colnot, M. Nakamura, Y. Wu, T. Miclau and R. S. Marcucio, *Dis. Models Mech.*, 2010, **3**, 451–458.

54 S. M. Hurst, T. S. Wilkinson, R. M. McLoughlin, S. Jones, S. Horiuchi, N. Yamamoto, S. Rose-John, G. M. Fuller, N. Topley and S. A. Jones, *Immunity*, 2001, **14**, 705–714.

55 L. J. Raggatt, M. E. Wullschleger, K. A. Alexander, A. C. Wu, S. M. Millard, S. Kaur, M. L. Maugham, L. S. Gregory, R. Steck and A. R. Pettit, *Am. J. Pathol.*, 2014, **184**, 3192–3204.

56 H. Takayanagi, K. Ogasawara, S. Hida, T. Chiba, S. Murata, K. Sato, A. Takaoka, T. Yokochi, H. Oda, K. Tanaka, K. Nakamura and T. Taniguchi, *Nature*, 2000, **408**, 600–605.

57 M. K. Chang, L. J. Raggatt, K. A. Alexander, J. S. Kuliwaba, N. L. Fazzalari, K. Schroder, E. R. Maylin, V. M. Ripoll, D. A. Hume and A. R. Pettit, *J. Immunol.*, 2008, **181**, 1232–1244.

58 F. Loi, L. A. Córdova, J. Pajarinen, T. Lin, Z. Yao and S. B. Goodmana, *Bone*, 2016, **86**, 119.

59 T. Yamaza, Y. Miura, Y. Bi, Y. Liu, K. Akiyama, W. Sonoyama, V. Patel, S. Gutkind, M. Young, S. Gronthos, A. Le, C. Y. Wang, W. Chen and S. Shi, *PLoS One*, 2008, **3**, e2615.

60 Y. Liu, L. Wang, T. Kikuiri, K. Akiyama, C. Chen, X. Xu, R. Yang, W. Chen, S. Wang and S. Shi, *Nat. Med.*, 2011, **17**, 1594.

61 Y. W. Ebright, Y. Chen, Y. G. Kim and R. H. Ebright, *Bioconjugate Chem.*, 1996, **7**, 380.

62 H. H. C. Lima, V. L. Kupfer, M. P. Moisés, M. R. Guilherme, J. C. Rinaldi, S. L. Felisbino, A. F. Rubira and A. W. Rinaldi, *Carbohydr. Polym.*, 2018, **196**, 126–134.

63 J. P. Schmitz and J. O. Hollinger, *Clin. Orthop. Relat. Res.*, 1986, 299.

64 A. S. DeConde, M. K. Lee, D. Sidell, T. Aghaloo, M. Lee, S. Tetradis, K. Low, D. Elashoff, T. Grogan, A. R. Sepahdari and M. St John, *JAMA Otolaryngol. Head Neck Surg.*, 2014, **140**, 58.

65 X. Fang, L. Lei, T. Jiang, Y. Chen and Y. Kang, *J. Biomed. Mater. Res., Part B*, 2018, **106**, 1739.

66 M. Yuan, Y. Zhan, W. Hu, Y. Li, X. Xie, N. Miao, H. Jin and B. Zhang, *Int. J. Mol. Med.*, 2018, **42**, 1967.

67 G. Paxinos, *The Rat Nervous System*, Elsevier Academic Press, San Diego, 2004.

68 W. Liang, X. Zhuo, Z. Tang, X. Wei and B. Li, *Mol. Cell. Biochem.*, 2015, **402**, 101.

69 L. Xiang, L. Ma, N. Wei, T. Wang, Q. Yao, B. Yang, Y. Xiong, Y. Wu and P. Gong, *Bone*, 2017, **94**, 135.

70 Y. Liu, G. Zheng, L. Liu, Z. Wang, Y. Wang, Q. Chen and E. Luo, *Cell Tissue Res.*, 2018, **59**, 147.

71 R. M. Hoerth, B. M. Seidt, M. Shah, C. Schwarz, B. M. Willie, G. N. Duda, P. Fratzl and W. Wagermaier, *Acta Biomater.*, 2014, **10**, 4009–4019.

72 S. Griffiths-Jones, R. J. Grocock, S. van Dongen, A. Bateman and A. J. Enright, *Nucleic Acids Res.*, 2006, **34**, D140.

73 R. Wu, Y. Tang, W. Zang, Y. Wang, M. Li, Y. Du, G. Zhao and Y. Xu, *Mol. Cell. Biochem.*, 2014, **387**, 151.

74 J. D. Klein and D. O. Fauza, *Methods Mol. Biol.*, 2011, **698**, 75.

75 K. J. Livak and T. D. Schmittgen, *Methods*, 2001, **25**, 402.

76 X. Chen and Z. Liu, *J. Mater. Chem. B*, 2016, **4**, 4382–4388.

77 Y. W. Ebright, Y. Chen, Y. G. Kim and R. H. Ebright, *Bioconjugate Chem.*, 1996, **7**, 380–384.

78 J. Chen, M. Liu, H. Gong, Y. Huang and C. Chen, *J. Phys. Chem. B*, 2011, **115**, 14947.

79 C. Wu, A. Ying and S. Ren, *Colloid Polym. Sci.*, 2013, **291**, 827.

80 X. Zhang, Y. Li, Y. F. Chen, J. Chen and P. X. Ma, *Nat. Commun.*, 2016, **7**, 10376.

81 Z. Liu, X. Chen, Z. Zhang, X. Zhang, L. Saunders, Y. Zhou and P. X. Ma, *ACS Nano*, 2018, **12**, 9785.

This journal is © The Royal Society of Chemistry 2019

J. Mater. Chem. B, 2019, **7**, 2722–2735 | **2735**